Published in final edited form as:
Appl Surf Sci. 2019 ; 471: 8–17. doi:10.1016/j.apsusc.2018.11.240.

Evaluation of the colloidal stability and adsorption performance of reduced graphene oxide–elemental silver/magnetite nanohybrids for selected toxic heavy metals in aqueous solutions

Chang Min Park[a,b,*], **Dengjun Wang**[b], **Jonghun Han**[c], **Jiyong Heo**[c], **Chunming Su**[d,**]

[a]Department of Environmental Engineering, Kyungpook National University, 80 Daehak-ro, Buk-gu, Daegu 41566, Republic of Korea

[b]National Research Council Resident Research Associate at the U.S. Environmental Protection Agency, 919 Kerr Research Drive, Ada, OK 74820, USA

[c]Department of Civil and Environmental Engineering, Korea Army Academy at Youngcheon, 495 Hogook-ro, Gokyungmeon, Youngcheon, Gyeongbuk 38900, Republic of Korea

[d]Groundwater, Watershed, and Ecosystem Restoration Division, National Risk Management Research Laboratory, Office of Research and Development, U.S. Environmental Protection Agency, 919 Kerr Research Drive, Ada, OK 74820, USA

Abstract

Reduced graphene oxide (rGO) hybridized with magnetite and/or elemental silver (rGO/magnetite, rGO/silver, and rGO/magnetite/silver) nanoparticles were evaluated as potential adsorbents for toxic heavy metal ions (Cd (II), Ni(II), Zn(II), Co(II), Pb(II), and Cu(II)). Although the deposition of iron oxide and silver nanoparticles on the rGO nanosheets played an inhibitory role in metal ion adsorption, the metal adsorption efficiency by the nanohybrids (NHs) was still higher than that reported for many other sorbents (e.g., activated biochar, commercial resins, and nanosized hydrated Zr(IV) oxide particles). X-ray photoelectron spectroscopy analyses revealed that complexation with deprotonated adsorbents and cation exchange was an important mechanism for Cd(II) ion removal by the rGO and NHs. Competitive adsorption tests using multi metals showed that the adsorption affinity of metal ions on the rGO and its NHs follows the order (Cu(II), Zn(II)) > Ni(II) > Co(II) > (Pb(II), Cd(II)), which is similar to the order observed for single-metal adsorption experiments. These results can be explained by the destabilization abilities of the rGO and NHs, as well as the ionic radii of the considered metal ions. Our findings demonstrate the feasibility of using rGO-based NHs as highly efficient adsorbents for heavy metal removal from water.

Keywords

Aggregation kinetics; Adsorption kinetics; Adsorption isotherms; Toxic heavy metal; XPS

[*]Corresponding author at: Department of Environmental Engineering, Kyungpook National University, 80 Daehak-ro, Buk-gu, Daegu 41566, Republic of Korea. [**]Corresponding author. cmpark@knu.ac.kr (C.M. Park), su.chunming@epa.gov (C. Su).

Introduction

Toxic heavy metals (e.g., cadmium, lead, nickel, copper, zinc, mercury, and chromium) are ranked as top priority pollutants on the U.S. Environmental Protection Agency's National Priorities List [1,2]. Heavy metal pollution poses potential long-term health risks for both the environment and human health, as they become bioavailable and thus toxic to living organisms with increasing exposure concentrations and periods [3]. Remediation of metal-contaminated sites is rather challenging because heavy metals cannot be degraded by (photo) catalysis or chemical reactions [4]. Among various conventional techniques including chemical precipitation [5], flocculation [6], membrane filtration [7], adsorption [8], etc., adsorption technologies are a promising choice as they are cost-saving and highly effective with no byproduct formation (i.e., they are eco-friendly) [9].

Recently, graphene-based nanomaterials have attracted considerable attention owing to their unique properties and multifunctionalities [10]. Once the graphene is oxidized, the oxygen-containing surface functional groups will be included like epoxide, hydroxyl, carbonyl, and carboxyl groups, residing along the basal planes or the edges of the structure. These oxygenated groups facilitate metal ion immobilization by strong complexation or cation exchange processes. Zare-Dorabei et al. [11] anchored 2,2′-dipyridylamine (DPA) as a bidentate coordination ligand on the graphene oxide (GO) to enhance functionalities. A large number of oxygen-containing functional groups on the GO-DPA increased the adsorption capacity for Cu(II) ions. Wu et al.[12] also showed that the abundant hydroxyl, carboxylic, and sulfonic groups on the 3D sulfonated reduced GO (3D-SRGO) aerogel strongly influenced the adsorption of Cd(II) ions. However, there still exist major hurdles for the practical use of those nanomaterials, including segregation difficulties after adsorption, relatively high aggregation propensities, and corresponding surface area reductions.

To overcome these challenges, metal/metal oxide nanoparticles have been incorporated into graphene as potential and cost-effective nano-adsorbents/catalysts [13–18]. In our previous study, the rGO/magnetite/silver was synthesized by co-precipitation method to alleviate rapid aggregation of nanoparticles, while enhancing the catalytic degradation efficiency for various micropollutants in the heterogeneous activation of peroxydisulfate [19,20]. According to the electrophoretic mobility measurements, the rGO/magnetite/silver bears a high negative charge density over the broad pH range (3–12) [20]. In addition, the aggregation of the rGO/magnetite/silver was significantly reduced due to the stronger electrostatic repulsion between the negatively-charged nanohybrids (NHs). This resulted in increased specific surface area and adsorption properties of the rGO/magnetite/silver. Taking all of these advantages into account, this multifunctional bimetallic rGO NH should be considered as an ideal alternative to remove the cationic heavy metal species.

This study investigated, for the first time, the effect of the deposition of iron oxide and silver nanoparticles onto rGO on the adsorption of divalent metal ions. Although some studies have investigated the adsorption of heavy metals on GO, these studies only reported the adsorption of a few selected metal ions on bare or modified GO, not accounting for the ionic radius effect of the adsorbates, which plays an important role in heavy metal adsorption [21].

The adsorption properties of rGO and NHs (with magnetite and silver nanoparticles) in single and mixed metal systems were examined and compared after careful characterization. Moreover, the X-ray photoelectron spectra of the rGO and NHs were analyzed to unravel the underlying interaction mechanisms between the rGO or the NHs and Cd(II) ions.

2. Materials and methods

2.1. Preparation of rGO, rGO/magnetite, rGO/silver, and rGO/magnetite/silver NHs

GO was prepared from natural graphite flakes (3061 grade, Asbury Graphite Mills) using a modified Hummers method [22]. The obtained GO was modified with ferric chloride hexahydrate ($FeCl_3 \cdot 6H_2O$) and silver nitrate ($AgNO_3$) to obtain rGO/magnetite, rGO/silver, and rGO/magnetite/silver, followed by reduction using a sodium borohydride ($NaBH_4$) aqueous solution as a reducing agent at room temperature (25 ± 0.5 °C). The obtained rGO, rGO/magnetite, rGO/silver, and rGO/magnetite/silver nanopowders were stored in an anaerobic glove box to prevent oxidation. The detailed procedure for synthesizing these NHs was described in our previous work [19]. $Cd(NO_3)_2$, $Ni(NO_3)_2$, Zn $(NO_3)_2$, $Co(NO_3)_2$, $Pb(NO_3)_2$, and $Cu(NO_3)_2$ reagents were purchased from Sigma-Aldrich Co. with a minimum purity of 99%. All other chemicals (*i.e.,* $Ca(NO_3)_2$, $KMnO_4$, H_2O_2, H_2SO_4, HCl, and NaOH) purchased from Sigma-Aldrich Co. were of reagent grade. Natural organic matter (NOM) (Suwannee River humic acid and fulvic acid) was purchased from International Humic Substance Society. DI water with a resistivity of > 18 MΩ/cm was obtained from a Milli-Q water treatment system (Millipore Co.) and was used to prepare all aqueous solutions.

2.2. Characterization of the synthesized adsorbents

The surface (zeta) potentials of rGO, rGO/magnetite, rGO/silver, and rGO/magnetite/silver NHs in suspension were measured as a function of pH using a light-scattering method on a ZetaSizer instrument (Nano ZS, Malvern Instruments). The pH was adjusted between 3.0 and 12.0 with 0.1 M HCl and 0.1 M NaOH. X-ray diffraction (XRD) patterns for the rGO and NHs were obtained on a Rigaku Miniflex II X-ray diffractometer with Mn-filtered Fe K_α radiation (λ = 0.1937 nm), operated at 30 kV and 15 mA. The rGO and NHs samples were scanned from 2θ of 20° to 90° in a 0.02° step increment. Peak analyses of the obtained XRD patterns were carried out using the Jade software package (Materials Data, Inc.), comparing the collected data to the Powder Diffraction File database of the JCPDS. The size and morphology of the rGO and NHs were observed using field-emission transmission electron microscopy (TEM). Samples for TEM measurements were prepared by dispersing the rGO and NHs in ultra-pure water under ultrasonication and depositing them onto carbon-coated TEM grids. TEM images showing their morphologies were recorded using a Titan G2 ChemiSTEM Cs Probe (FEI Co.) operated at 200 keV. Fourier transform-infrared (FT-IR) spectra of unsorbed and Cd(II) sorbed rGOs and NHs were recorded on a Nicolet 6700 FT-IR spectrometer (Thermo Scientific, Inc.) for wavenumbers between 4000 and 400 cm^{-1}. The X-ray photoelectron spectra (XPS) of unsorbed and Cd(II) sorbed rGOs and NHs were determined using a PHI Quantera SXM scanning X-ray microscope (ULVAC-PHI, Inc.).

2.3. Equilibrium and kinetic adsorption experiments

A fixed amount (0.2 g/L) of rGO or NHs was mixed with Cd(II), Ni (II), Zn(II), Co(II), Pb(II), and Cu(II) solutions, containing 10 mM $NaNO_3$ as a background electrolyte for 24 h at room temperature. Aliquots of solution were periodically withdrawn at various time intervals for the kinetic study. The collected samples were then filtered using a 0.45-μm pore-size membrane filter, and the Cd(II), Ni(II), Zn(II), Co(II), Pb(II), and Cu(II) concentrations in filtered solutions were determined by an inductively coupled plasma-mass spectrometry (ICP-MS, Agilent 7900, Agilent Technologies). The desired pH values of adsorbates were adjusted using 0.01 M HCl or 0.01 M NaOH. The effects of NOM (5 mg/L of Suwannee River humic and fulvic acids) on the adsorption of heavy metal ions by rGO and NHs were investigated in a multi-metal system containing 1 mM of Cu(II), Ni(II), Zn(II), Co(II), Pb (II), and Cu(II) mixtures at 10 mM of $NaNO_3$. All adsorption experiments were conducted in duplicate.

Changes in average hydrodynamic diameters (HDDs) of the rGO and NHs were examined as a function of heavy metal ion concentrations. Time-resolved dynamic light scattering (TRDLS) was employed to record the aggregation kinetics of the rGO and NHs using the ZetaSizer (Nano ZS, Malvern Instruments) [23]. All TRDLS measurements were performed at a scattering angle of 173° over a period of 20 min to acquire a large enough increase in the HDDs. Autocorrelation functions were accumulated for 15 s, and the intensity-weighted HDDs were derived by second-order cumulant analysis. The early-stage aggregation kinetics for the rGO and NHs were obtained from the initial rate of change (k) in the HDD with time, t:

$$k \propto \frac{1}{N_0}\left(\frac{\mathrm{d}D_h(t)}{\mathrm{d}t}\right)_{t\to 0} \quad (1)$$

where N_0 represents the initial rGO or NH concentration in suspension [24], and D_h represents the HDD. A linear regression analysis was employed to obtain $(\mathrm{d}D_\mathrm{h}(t)/\mathrm{d}t)_{t\to 0}$ over the period in which HDD reached 1.5 times of the initial HDD [24,25].

3. Results and discussion

3.1. Characterization of rGO and NHs

TEM analyses were conducted to confirm the successful deposition of iron oxide and silver nanoparticles on the surface of the rGO via *in situ* nucleation and crystallization (Fig. 1). The magnetic rGO/magnetite and rGO/magnetite/silver showed the formation of clustered and distributed regions of iron oxides over the visible surface of the rGO nanosheet (Fig. 1b, d). A sphere-like structure was grown, which is indicative of a high degree of entanglement for the iron oxides and silver in rGO/magnetite/silver. Our previous study [20] reported that rGO/magnetite/silver exhibited less aggregation (an effective diameter 220–300 nm) than rGO and rGO/magnetite in the aqueous electrolyte solution (5–100 mM NaCl). The dispersion of magnetic iron oxide and silver on the thin layers (ca. 1 nm thick [26,27]) of the rGO, however, decreases the number of sites available for the sorption of heavy metal ions,

which affects the accessibility of active surface sites for aqueous metallic ions and the kinetic and equilibrium behaviors of the sorption process.

XRD patterns for the rGO and NHs are shown in Fig. 2. A strong peak at 32.6° (2θ), with 3.45 Å interlayer spacing, was observed for rGO, which is attributed to the pristine graphite (0 0 2) plane (JCPDS Number 01-089-8487). The strong peak at 32.2° for rGO/magnetite is attributed to pristine graphite (0 0 2). Multiple broad magnetite peaks for rGO/magnetite were also observed, which are in good agreement with the XRD pattern for magnetite (JCPDS No. 01-075-0449). The sharp peaks centered at 48.6°, 56.7°, and 84.3° are attributed to the silver-3C, syn. (1 1 1), (2 0 0), and (2 2 0) planes, respectively (JCPDS No. 01-087-0597), as confirmed by the presence of silver nanoparticles on both the rGO/silver and rGO/magnetite/silver surfaces. A small diffraction peak at 45.5° (2θ) for rGO/magnetite/silver, corresponding to the magnetite (3 1 1) plane, demonstrated compressive loadings of Ag(I) on the surface of the rGO nanosheet [28].

The zeta potentials of the rGO and NHs were measured at various pH values at room temperature (Fig. 3). The results showed that all zeta potentials values were negative for pH levels of 3.0–10 owing to the deportation of carboxylic and phenolic functional groups [29]. The zeta potentials changed slightly with pH ranges of 3.0–6.0, which indicates a strong aggregation tendency in acidic and weakly acidic conditions. The zeta potential became significantly more negative when the pH > 6.0. Therefore, the rGO and NHs were negatively charged under environmentally relevant pH conditions, which will facilitate the sorption of positively charged metallic ions.

3.2. Cd(II) adsorption by rGO and NHs

3.2.1. Adsorption kinetics—Cd(II) adsorption characteristics by rGO and NHs were compared by varying the reaction time from 10 s to 150 min (Fig. 4a). Cd(II) was chosen here for further equilibrium adsorption isotherm and kinetic experiments because the adsorption capacities of Cd(II) on the rGO, rGO/magnetite, rGO/silver, and rGO/magnetite/silver were relatively low at pH 4. The Cd(II) adsorption capacity followed the order rGO > rGO/magnetite/silver > rGO/silver > rGO/magnetite. rGO showed the highest adsorption performance and the shortest time required to achieve adsorption equilibrium (80.5% within 5 min) compared with the other rGO-based NHs. After the initial rapid adsorption, the rate of adsorption slowed down over the next 25 min, accounting for 16.2% of the final adsorption capacity (3.835 mmol/g). rGO/magnetite exhibited the smallest adsorption capacity (2.569 mmol/g) and the slowest Cd(II) adsorption rate (57.8% within 5 min). In the rGO/silver and rGO/magnetite/silver systems, 2.089 and 2.712 mmol/g of Cd(II), respectively, were rapidly adsorbed within 5 min, accounting for 62.9% and 79.7%, respectively, of the maximum adsorption capacities.

These results indicated that the iron and elemental silver-deposited rGOs may play an inhibitory role in the adsorption of Cd(II) ions. Therefore, the rGO with no metal deposition is better for Cd(II) immobilization owing to the weak electrostatic repulsion between rGO and Cd(II). The differences in the adsorption kinetics between rGO and NHs were positively correlated with the aggregation rates of these NHs for Cd(II) ions, except for rGO/magnetite, which has magnetic properties that promote particle aggregation. Cd(II) ions in solution may

induce bridging of bare rGO nanosheets, which leads to both greater adsorption of Cd(II) on rGO and higher aggregation rates for rGO compared with metal-loaded rGOs [30,31].

To probe the underlying Cd(II) adsorption mechanisms by the rGO and NHs, linearized pseudo-first-order [32] and pseudo-second-order kinetic models [33] were employed, as expressed in Eqs. (2) and (3), respectively:

$$\ln(q_e - q_t) = \ln q_e - k_1 t \tag{2}$$

$$\frac{1}{q_t} = \frac{1}{k_2 q_e^2} \cdot \frac{1}{t} + \frac{1}{q_e} \tag{3}$$

where q_t (mmol/g) and q_e (mmol/g) are the amounts of Cd(II) adsorbed at time t and at equilibrium, respectively and k_1 and k_2 are the pseudo-first-order and pseudo-second-order rate constants of adsorption (1/min), respectively, which can be calculated from a plot of ln ($q_e - q_t$) versus t and $1/q_t$ versus $1/t$, respectively. The amounts of Cd(II) adsorbed on the rGO and NHs were calculated using Eq. (4):

$$q_e = \left[C_0 - C_e \frac{V}{m}\right] \tag{4}$$

where C_0 (mmol/L) refers to the initial concentration of Cd(II) ion, C_e (mmol/L) is the Cd(II) concentration in the aqueous solution at equilibrium, m is the mass of the adsorbents (g), and V is the volume of the suspension (L). The calculated parameters of the pseudo-first-order and pseudo-second-order kinetic models are shown in Table S2. The correlation coefficient values (r^2) for the pseudo-second-order kinetic model were higher than those obtained from the pseudo-first-order kinetic model simulations. This result suggested that the Cd(II) adsorption processes for the rGO and NHs were better described by the pseudo-second-order model, which has also been observed for Cd(II) adsorption by other GO-based nanosheets, such as GO [34], functionalized graphene [35], magnetic graphene oxide [36], 2,2′-dipyridylamine modified GO [11], amino functionalized magnetic graphene composite [37], and 3D-SRGO [12]. According to the pseudo-second-order model assumptions, the rate-limiting step of Cd(II) ion adsorption can be attributed to the chemical adsorption (chemisorption) via bonding forces through electron sharing or exchange between the rGO or NHs and Cd(II) ions (see Scheme 1) [38].

3.2.2. Adsorption isotherms—Batch experiments were conducted by varying Cd(II) ion concentrations from 0.01 to 4 mM to investigate adsorption isotherms (Fig. 4b). To further explain the macroscopic interaction mechanisms of the rGO and NHs with Cd(II) ions, Langmuir and Freundlich isotherm models were used to describe the Cd(II) adsorption data at room temperature [39,40]. The Langmuir isotherm model, which assumes uniform adsorption energy and monolayer coverage on the adsorbent, can be expressed by Eq. (5) as follows [41]:

$$\frac{1}{q_e} = \frac{1}{q_m} + \frac{1}{k_L q_m C_e} \tag{5}$$

$$R_L = \frac{1}{1 + C_0 k_L} \quad (6)$$

where q_m (mmol/g) is the maximum adsorption capacity and k_L (L/mmol) is the equilibrium constant of the reaction that reflects the adsorption binding energy. The Freundlich isotherm model describes Cd(II) ion adsorption on a heterogeneous rGO or NH surface by multilayer adsorption. The empirical linear equation can be expressed by Eq. (7) as follows [42]:

$$\ln q_e = \ln k_f + \frac{1}{n} \ln C_e \quad (7)$$

where k_f is Freundlich affinity coefficient and $1/n$ is the intensity of the adsorption ($1 < n < 10$). The larger the calculated value of n, the greater the expected heterogeneity of the adsorption sites. The non-linear Chi-square (χ^2) test was used to evaluate the fit of the isotherms to the experimental data [43]. The χ^2 test statistic is defined as the sum of the squares of the differences between the experimental data and theoretically calculated data from isotherm models. The equivalent mathematical statement (Eq. (8)) is

$$\chi^2 = \sum \frac{\left(q_e^{exp} - q_e^{cal}\right)^2}{q_e^{cal}} \quad (8)$$

where q_e^{exp} (mmol/g) is the experimental data for the adsorption capacity at equilibrium and q^{cal} (mmol/g) is the equilibrium capacity calculated from the isotherm models. If the χ^2value obtained is smaller, the calculated values are closer to the experimental data. Analyses of the experimental data using the χ^2 test are necessary to confirm the best-fit isotherms. The isotherm model parameters are listed in Table S3.

The adsorption isotherms for the rGO and NHs were better fitted by the Langmuir isotherm model, considering that the χ^2 values for the Langmuir model were much smaller than those for the Freundlich model. These results suggested that the adsorption of Cd(II) ions on rGO, rGO/magnetite, rGO/silver, and rGO/magnetite/silver followed monolayer adsorption processes. The Freundlich isotherm model was unsuitable for interpreting the experimental data owing to the relatively low correlation coefficient ($r^2 < 0.91$) [44]. rGO had a higher Cd(II) adsorption capacity (3.854 mmol/g) than many other rGO-based sorbents reported elsewhere, including 3D-SRGO having high affinity between sulfo groups and heavy metals (2.089 mmol/g) [12] and nano zerovalent iron supported on rGO having enhanced dispersion ability and stability (3.787 mmol/g) [45] (Table 1). The high adsorption capacities of the rGO and NHs for Cd(II) ions can be explained by the oxygenated functional groups having a lone electron pair to share with a metallic ion, forming a metal–rGO surface complex [34]. Although the deposition of magnetite on rGO (*i.e.,* rGO/magnetite (q_m = 2.605 mmol/g)) decreased 32.4% of the maximum Cd(II) adsorption capacity for bare rGO, further hybridization with silver (*i.e.,* rGO/magnetite/silver (q_m = 3.441 mmol/g)) can compensate for the adsorptive capacity (32.1% enhancement). The rGO synthesized with silver only (*i.e.* rGO/silver (q_m = 3.317 mmol/g)) slightly decreased the adsorption performance compared with bare rGO (13.9% decrease). However, the q_m values for rGO/magnetite, rGO/silver, and rGO/magnetite/silver were still higher than the sorbents described above (*i.e.,* activated

biochar, Amberlite IRC-718, α-KA-Fe_3O_4/CS, and NZPs). These results suggested that magnetite-and silver-deposited rGO nanosheets possess significant potential for use in heavy metal removal in wastewater cleanup.

3.3. XPS study of the adsorption of Cd(II) on rGO and NHs

To confirm the chemisorption characteristics of Cd(II) ions on the rGO and NHs, XPS measurements were carried out before and after adsorption experiments. XPS spectra obtained for the bare rGO are shown in Fig. 5 and Table S4. The high-resolution C1s spectra of rGO showed that significant differences in both peak shape and peak intensity were observed before and after Cd(II) adsorption. The strong peak in the C1s spectrum is attributed to C-C aromatic bonds with binding energies of 284.3 eV. The second largest peak (286.1 eV) formed after Cd(II) adsorption on rGO can be ascribed to the carbon atom of the amino group (C-NH_2). The peak intensity of the O1s spectrum for rGO before Cd(II) adsorption differs significantly from that of the spectrum with adsorbed Cd(II) ions. The O1s peak for rGO with adsorbed Cd(II) ions at approximately 531.8 eV, presumably arising from C=O bonds, increased in intensity, providing evidence that the oxygen-containing functional groups were strongly associated with the adsorption of Cd(II) ions on rGO. The Cd3d spectrum of rGO with adsorbed Cd(II) ions had noticeable peaks at approximately 405.7 and 412.3 eV, which signifies successful Cd(II) binding to the rGO (Fig. 5d) due to complexation with deprotonated sites on rGO and cation exchange (see reactions (5) and (6)).

3.4. Aggregation kinetics of rGO and NHs

To test the effect of heavy metal adsorption on the stability of rGO and NHs, the aggregation kinetic profiles were investigated as a function of Cd(II), Ni(II), Zn(II), Co(II), Pb(II), and Cu(II) ion (Fig. 6). The concentrations of the rGO and NHs were controlled at 0.2 g/L, which is consistent with the batch adsorption experiments. The increase in the rate of aggregation can be attributed to the compression and charge screening of electrostatic double-layer of nanoparticles [46]. Although divalent cations showed a similar degree of charge screening according to the Schulze–Hardy rule [47,48], the heavy metals displayed destabilization abilities for the rGO and NHs in the following order: Cu(II) > Zn(II) > Ni(II) > Co(II) > Cd(II), Pb(II). The aggregation rate plots in Fig. S2 correspond to the adsorption capacities of heavy metal ions by the rGO and NHs. This result indicated that the destabilization of the rGO and NHs by heavy metal ions was a combined process involving adsorption and ionic radius effects [46]. However, the aggregation rate for rGO/magnetite increased notably despite the lower adsorption capacity for metal ions compared with rGO, rGO/silver, and rGO/magnetite/silver (Fig. S1). This result can be attributed to the magnetic properties of the rGO/magnetite and lower zeta potentials when heavy metal ions were added to the suspension.

Further analysis revealed that the stability of the rGO and NHs was highly dependent on the type and concentration of the divalent cations. The zeta potentials of the rGO and NHs as a function of heavy metal ion concentrations are shown in Fig. S3. The surface negativities of rGO/silver and rGO/magnetite/silver decreased as the metal ion concentrations increased, exerting a screening effect on the electrostatic potentials, although the differences in zeta potentials were negligible for rGO and rGO/magnetite. This meant that rGO/silver and rGO/

magnetite/silver NHs were stably dispersed in water in the presence of metal ions, whereas rGO and rGO/magnetite were present in a more aggregated form.

3.5. Adsorption in a multi-metal mixture

The differences in the affinity of metal ions for the rGO and NHs were observed for a multi-metal mixture. For this purpose, the competitive adsorption of six aqueous metal cations (Cu/Ni/Zn/Co/Pb/Cu mixtures) was examined with the same initial concentration of metallic ions (5.0 μmol per 1 mg of rGO, rGO/magnetite, rGO/silver, and rGO/magnetite/silver). Fig. 7 shows the experimental data for the multi-metal mixtures and the relative amounts of adsorbed metal ions. It should be noted that the adsorption capacities of metal ions on the rGO and NHs significantly decreased in the multi-metal mixture compared with those in the single-metal system (Fig. S1). However, the rGO and NHs still exhibited a greater preference for Zn(II) (16.780–22.639% of the total adsorption) and Cu(II) (22.638–25.871% of the total adsorption) than Cd(II), Ni(II), Co(II), and Pb(II). In competitive adsorption of Cd(II), Ni(II), Zn(II), Co(II), Pb(II), and Cu(II), the adsorption affinity on the rGO and NHs followed the order (Cu(II), Zn(II) > Ni(II) > Co(II) > Pb(II), Cd(II)). This order matches the ionic radii of these metal ions (i.e., Cd(II), Ni(II), Zn(II), Co(II), Pb(II), and Cu(II)), as in the single-metal systems.

The adsorption capacity and selectivity of the rGO and NHs for Cd (II), Ni(II), Zn(II), Co(II), Pb(II), and Cu(II) ions were also investigated under optimized conditions and in the presence of NOM, which is ubiquitously present in surface water and, in general, exhibits adverse effects in water treatment process. The adsorption capacities obtained according to the type of NOM and the percentage increase are summarized in Table S5. Suwannee River humic and fulvic acids significantly enhanced the adsorption efficiency of Cd(II), Ni(II), Co(II), and Pb(II), particularly for rGO/magnetite. The increased adsorption percentage in the presence of NOM can be attributed to the formation of strong complexes consisting of metal ions and the NOM carboxylic and phenolic groups adsorbed on the available sites of the rGO and NHs [49]. NOM can effectively disperse the rGO and NHs, so their available surface areas increase compared to those without presence of NOM, this may be another reason for the observed results. When Zn(II) and Cu(II) ions were present, however, the differences in the adsorption capacities were not significant, suggesting that the adsorption efficiency was not seriously influenced by the NOM species.

4. Conclusions

The unique properties of rGO attract particular interest in the context of heavy metal removal owing to their abundant oxygenated functional groups. These surface groups facilitate the binding of metal ions by complexation with rGO and NHs owing to electron pair sharing. The decoration of magnetite and silver nanoparticles on the surface of rGO decreased the adsorption affinity of metal ions, but adsorption capacities for metal ions remained high at 3.854, 2.605, 3.317, and 3.441 mmol/g for rGO, rGO/magnetite, rGO/silver, and rGO/magnetite/silver NHs, respectively, towards Cd(II). These values are greater than the adsorption capacities recently reported for other sorbents. The single-metal and competitive adsorption studies showed that the affinities of rGO and NHs for these metal

ions decreased in the order of Cu (II) ≈ Zn(II) > Ni(II) > Co(II) > Cd(II), Pb(II). The affinity order corresponds to the destabilization ability of rGO and its NHs and the ionic radius order of the metal ions. The kinetics of Cd(II) adsorption on the rGO and NHs were better described by the pseudo-second-order model than the pseudo-first-order model, suggesting that the adsorption process was controlled by chemisorption including surface complexation between Cd(II) ions and adsorbents. The adsorption isotherms for metal ions on rGO and NHs were fitted better by the Langmuir model than by the Freundlich model, which suggests that the adsorption process involves monolayer coverage with uniform adsorption energy. XPS analysis confirmed that complexation with deprotonated sites of the adsorbents and cation exchange of sodium/hydrogen by Cd(II) were the major mechanisms for the removal of Cd(II) ions. Taking into consideration the slight decrease in the adsorptive performance for heavy metal ions, the rGO-based NHs with magnetite and elemental silver could be applicable for metal decontamination.

Supplementary Material

Refer to Web version on PubMed Central for supplementary material.

Acknowledgments

This study was supported by the U.S. Environmental Protection Agency, the Basic Science Research Program through the National Research Foundation of Korea (NRF) funded by the Ministry of Education (NRF-2018R1A6A1A03024962 and NRF-2018R1D1A1B07040341), and the Korea Ministry of Environment (The SEM projects; 2018002470005). The views expressed in this article are those of the authors and do not necessarily represent the views or policies of the U.S. Environmental Protection Agency.

References

[1]. Mulligan C, Yong R, Gibbs B, Remediation technologies for metal-contaminated soils and groundwater: an evaluation, Eng. Geol 60 (2001) 193–207.

[2]. Cameron R, Guide to site and soil description for hazardous waste site characterization, Metals, Environmental Protection Agency EPA/600/4–91/029, (1992).

[3]. Liu X, Song Q, Tang Y, Li W, Xu J, Wu J, Wang F, Brookes PC, Human health risk assessment of heavy metals in soil–vegetable system: a multi-medium analysis, Sci. Total Environ 463 (2013) 530–540. [PubMed: 23831799]

[4]. Rajkumar M, Ae N, Prasad MNV, Freitas H, Potential of siderophore-producing bacteria for improving heavy metal phytoextraction, Trends Biotechnol. 28 (2010) 142–149. [PubMed: 20044160]

[5]. Uluozlu OD, Tuzen M, Mendil D, Soylak M, Coprecipitation of trace elements with Ni^{2+}/2-Nitroso-1-naphthol-4-sulfonic acid and their determination by flame atomic absorption spectrometry, J. Hazard. Mater 176 (2010) 1032–1037. [PubMed: 20022172]

[6]. Karbassi A, Nadjafpour S, Flocculation of dissolved Pb, Cu, Zn and Mn during estuarine mixing of river water with the Caspian Sea, Environ. Pollut 93 (1996) 257–260. [PubMed: 15093524]

[7]. Soylak M, Unsal YE, Kizil N, Aydin A, Utilization of membrane filtration for preconcentration and determination of Cu(II) and Pb(II) in food, water and geological samples by atomic absorption spectrometry, Food Chem. Toxicol 48 (2010) 517–521. [PubMed: 19913067]

[8]. Hao L, Song H, Zhang L, Wan X, Tang Y, Lv Y, SiO_2/graphene composite for highly selective adsorption of Pb(II) ion, J. Colloid Interface Sci 369 (2012) 381–387. [PubMed: 22218342]

[9]. Park CM, Han J, Chu KH, Al-Hamadani YA, Her N, Heo J, Yoon Y, Influence of solution pH, ionic strength, and humic acid on cadmium adsorption onto activated biochar: Experiment and modeling, J. Ind. Eng. Chem 48 (2017) 186–193.

[10]. McAllister MJ, Li J-L, Adamson DH, Schniepp HC, Abdala AA, Liu J, Herrera-Alonso M, Milius DL, Car R, Prud'homme RK, Single sheet functionalized graphene by oxidation and thermal expansion of graphite, Chem. Mater 19 (2007) 4396–4404.

[11]. Zare-Dorabei R, Ferdowsi SM, Barzin A, Tadjarodi A, Highly efficient simultaneous ultrasonic-assisted adsorption of Pb(II), Cd(II), Ni(II) and Cu(II) ions from aqueous solutions by graphene oxide modified with 2, 2′-dipyridylamine: central composite design optimization, Ultrason. Sonochem 32 (2016) 265–276. [PubMed: 27150770]

[12]. Wu S, Zhang K, Wang X, Jia Y, Sun B, Luo T, Meng F, Jin Z, Lin D, Shen W, Enhanced adsorption of cadmium ions by 3D sulfonated reduced graphene oxide, Chem. Eng. J 262 (2015) 1292–1302.

[13]. Yang X, Chen W, Huang J, Zhou Y, Zhu Y, Li C, Rapid degradation of methylene blue in a novel heterogeneous Fe_3O_4@rGO@TiO_2-catalyzed photo-Fenton system, Sci. Rep 5 (2015) 10632. [PubMed: 26000975]

[14]. Zhang N, Qiu H, Liu Y, Wang W, Li Y, Wang X, Gao J, Fabrication of gold nanoparticle/graphene oxide nanocomposites and their excellent catalytic performance, J. Mater. Chem 21 (2011) 11080–11083.

[15]. Queraltó A, del Pino AP, Logofatu C, Datcu A, Amade R, Bertran-Serra E, György E, Reduced graphene oxide/iron oxide nanohybrid flexible electrodes grown by laser-based technique for energy storage applications, Ceram. Int 44 (2018) 20409–20416.

[16]. Huang J, Chang Q, Ding Y, Han X, Tang H, Catalytic oxidative removal of 2, 4-dichlorophenol by simultaneous use of horseradish peroxidase and graphene oxide/Fe_3O_4 as catalyst, Chem. Eng. J 254 (2014) 434–442.

[17]. Chen J, Sun L, Cheng Y, Lu Z, Shao K, Li T, Hu C, Han H, Graphene oxide-silver nanocomposite: novel agricultural antifungal agent against *Fusarium graminearum* for crop disease prevention, ACS Appl. Mater. Interfaces 8 (2016) 24057–24070. [PubMed: 27563750]

[18]. Queraltó A, del Pino ÁP, Logofatu C, Datcu A, Amade R, Alshaikh I, Bertran E, Urzica I, György E, MAPLE synthesis of reduced graphene oxide/silver nanocomposite electrodes: Influence of target composition and gas ambience, J. Alloys Compd 726 (2017) 1003–1013.

[19]. Park CM, Heo J, Wang D, Su C, Yoon Y, Heterogeneous activation of persulfate by reduced graphene oxide–elemental silver/magnetite nanohybrids for the oxidative degradation of pharmaceuticals and endocrine disrupting compounds in water, Appl. Catal., B 225 (2018) 91–99. [PubMed: 32704206]

[20]. Park CM, Wang D, Heo J, Her N, Su C, Aggregation of reduced graphene oxide and its nanohybrids with magnetite and elemental silver under environmentally relevant conditions, J. Nanopart. Res 20 (2018) 93. [PubMed: 31595146]

[21]. Gao Z, Bandosz TJ, Zhao Z, Han M, Qiu J, Investigation of factors affecting adsorption of transition metals on oxidized carbon nanotubes, J. Hazard. Mater 167 (2009) 357–365. [PubMed: 19264402]

[22]. Chen C, Yang QH, Yang Y, Lv W, Wen Y, Hou PX, Wang M, Cheng HM, Self-assembled free-standing graphite oxide membrane, Adv. Mater 21 (2009) 3007–3011.

[23]. Zheng T, Bott S, Huo Q, Techniques for accurate sizing of gold nanoparticles using dynamic light scattering with particular application to chemical and biological sensing based on aggregate formation, ACS Appl. Mater. Interfaces 8 (2016) 21585–21594. [PubMed: 27472008]

[24]. Chen KL, Elimelech M, Aggregation and deposition kinetics of fullerene (C_{60}) nanoparticles, Langmuir 22 (2006) 10994–11001. [PubMed: 17154576]

[25]. Chen KL, Elimelech M, Influence of humic acid on the aggregation kinetics of fullerene (C60) nanoparticles in monovalent and divalent electrolyte solutions, J. Colloid Interface Sci 309 (2007) 126–134. [PubMed: 17331529]

[26]. Stankovich S, Dikin DA, Dommett GH, Kohlhaas KM, Zimney EJ, Stach EA, Piner RD, Nguyen ST, Ruoff RS, Graphene-based composite materials, Nature 442 (2006) 282–286. [PubMed: 16855586]

[27]. Liu W, Ma J, Shen C, Wen Y, Liu W, A pH-responsive and magnetically separable dynamic system for efficient removal of highly dilute antibiotics in water, Water Res. 90 (2016) 24–33. [PubMed: 26724436]

[28]. Bandyopadhyay R, Selbo J, Amidon GE, Hawley M, Application of powder X-ray diffraction in studying the compaction behavior of bulk pharmaceutical powders, J. Pharm. Sci 94 (2005) 2520–2530. [PubMed: 16200547]

[29]. Bhadra BN, Seo PW, Jhung SH, Adsorption of diclofenac sodium from water using oxidized activated carbon, Chem. Eng. J 301 (2016) 27–34.

[30]. Yu S, Wang X, Ai Y, Liang Y, Ji Y, Li J, Hayat T, Alsaedi A, Wang X, Spectroscopic and theoretical studies on the counterion effect of Cu(II) ion and graphene oxide interaction with titanium dioxide, Environ. Sci. Nano 3 (2016) 1361–1368.

[31]. Liu X, Pan L, Lv T, Zhu G, Sun Z, Sun C, Microwave-assisted synthesis of CdS–reduced graphene oxide composites for photocatalytic reduction of Cr(VI), Chem. Commun 47 (2011) 11984–11986.

[32]. Doğan M, Alkan M, Demirbaş Ö, Özdemir Y, Özmetin C, Adsorption kinetics of maxilon blue GRL onto sepiolite from aqueous solutions, Chem. Eng. J 124 (2006) 89–101.

[33]. Ho Y-S, Review of second-order models for adsorption systems, J. Hazard. Mater 136 (2006) 681–689. [PubMed: 16460877]

[34]. Sitko R, Turek E, Zawisza B, Malicka E, Talik E, Heimann J, Gagor A, Feist B, Wrzalik R, Adsorption of divalent metal ions from aqueous solutions using graphene oxide, Dalton Trans. 42 (2013) 5682–5689. [PubMed: 23443993]

[35]. Deng X, Lü L, Li H, Luo F, The adsorption properties of Pb(II) and Cd(II) on functionalized graphene prepared by electrolysis method, J. Hazard. Mater 183 (2010) 923–930. [PubMed: 20800353]

[36]. Deng J-H, Zhang X-R, Zeng G-M, Gong J-L, Niu Q-Y, Liang J, Simultaneous removal of Cd(II) and ionic dyes from aqueous solution using magnetic graphene oxide nanocomposite as an adsorbent, Chem. Eng. J 226 (2013) 189–200.

[37]. Guo X, Du B, Wei Q, Yang J, Hu L, Yan L, Xu W, Synthesis of amino functionalized magnetic graphenes composite material and its application to remove Cr (VI), Pb(II), Hg(II), Cd(II) and Ni(II) from contaminated water, J. Hazard. Mater 278 (2014) 211–220. [PubMed: 25016452]

[38]. Zhou N, Chen H, Xi J, Yao D, Zhou Z, Tian Y, Lu X, Biochars with excellent Pb(II) adsorption property produced from fresh and dehydrated banana peels via hydrothermal carbonization, Bioresour. Technol 232 (2017) 204–210. [PubMed: 28231538]

[39]. Dada A, Olalekan A, Olatunya A, Dada O, Langmuir, Freundlich, Temkin and Dubinin-Radushkevich isotherms studies of equilibrium sorption of Zn^{2+} unto phosphoric acid modified rice husk, J. Appl. Chem 3 (2012) 38–45.

[40]. Park CM, Chu KH, Heo J, Her N, Jang M, Son A, Yoon Y, Environmental behavior of engineered nanomaterials in porous media: a review, J. Hazard. Mater 309 (2016) 133–150. [PubMed: 26882524]

[41]. Cheng M, Zeng G, Huang D, Lai C, Xu P, Zhang C, Liu Y, Hydroxyl radicals based advanced oxidation processes (AOPs) for remediation of soils contaminated with organic compounds: a review, Chem. Eng. J 284 (2016) 582–598.

[42]. Uçar S, Erdem M, Tay T, Karagöz S, Removal of lead(II) and nickel(II) ions from aqueous solution using activated carbon prepared from rapeseed oil cake by Na_2CO_3 activation, Clean Technol. Environ. Policy 17 (2015) 747–756.

[43]. Yu Y, Yu L, Chen JP, Adsorption of fluoride by Fe–Mg–La triple-metal composite: adsorbent preparation, illustration of performance and study of mechanisms, Chem. Eng. J 262 (2015) 839–846.

[44]. Guo F-Y, Liu Y-G, Wang H, Zeng G-M, Hu X-J, Zheng B-H, Li T-T, Tan X-F, Wang S-F, Zhang M-M, Adsorption behavior of Cr(VI) from aqueous solution onto magnetic graphene oxide functionalized with 1, 2-diaminocyclohexanetetraacetic acid, RSC Adv. 5 (2015) 45384–45392.

[45]. Vaughan T, Seo CW, Marshall WE, Removal of selected metal ions from aqueous solution using modified corncobs, Bioresour. Technol 78 (2001) 133–139. [PubMed: 11333031]

[46]. Yang K, Chen B, Zhu X, Xing B, Aggregation, adsorption, and morphological transformation of graphene oxide in aqueous solutions containing different metal cations, Environ. Sci. Technol 50 (2016) 11066–11075. [PubMed: 27662468]

[47]. Sano M, Okamura J, Shinkai S, Colloidal nature of single-walled carbon nanotubes in electrolyte solution: the Schulze– Hardy rule, Langmuir 17 (2001) 7172–7173.

[48]. Lide DR, CRC Handbook of Chemistry and Physics, CRC Press/Taylor and Francis, Boca Raton, FL, 2012.

[49]. Yang S, Hu J, Chen C, Shao D, Wang X, Mutual effects of Pb(II) and humic acid adsorption on multiwalled carbon nanotubes/polyacrylamide composites from aqueous solutions, Environ. Sci. Technol 45 (2011) 3621–3627. [PubMed: 21395259]

[50]. Vuković GD, Marinković AD, Čolić M, Ristić MĐ, Aleksić R, Perić-Grujić AA, Uskoković PS, Removal of cadmium from aqueous solutions by oxidized and ethylenediamine-functionalized multi-walled carbon nanotubes, Chem. Eng. J 157 (2010) 238–248.

[51]. Boparai HK, Joseph M, O'Carroll DM, Kinetics and thermodynamics of cadmium ion removal by adsorption onto nano zerovalent iron particles, J. Hazard. Mater 186 (2011) 458 [PubMed: 21130566]

[52]. Gupta V, Nayak A, Cadmium removal and recovery from aqueous solutions by novel adsorbents prepared from orange peel and Fe_2O_3 nanoparticles, Chem. Eng. J 180 (2012) 81–90.

[53]. Yang G, Tang L, Lei X, Zeng G, Cai Y, Wei X, Zhou Y, Li S, Fang Y, Zhang Y, Cd(II) removal from aqueous solution by adsorption on α-ketoglutaric acid-modified magnetic chitosan, Appl. Surf. Sci 292 (2014) 710–716.

[54]. Li J, Chen C, Zhu K, Wang X, Nanoscale zero-valent iron particles modified on reduced graphene oxides using a plasma technique for Cd(II) removal, J. Taiwan Inst. Chem. Eng 59 (2016) 389–394.

[55]. Ahmad Z, Gao B, Mosa A, Yu H, Yin X, Bashir A, Ghoveisi H, Wang S, Removal of Cu(II), Cd(II) and Pb(II) ions from aqueous solutions by biochars derived from potassium-rich biomass, J. Cleaner Prod 180 (2018) 437

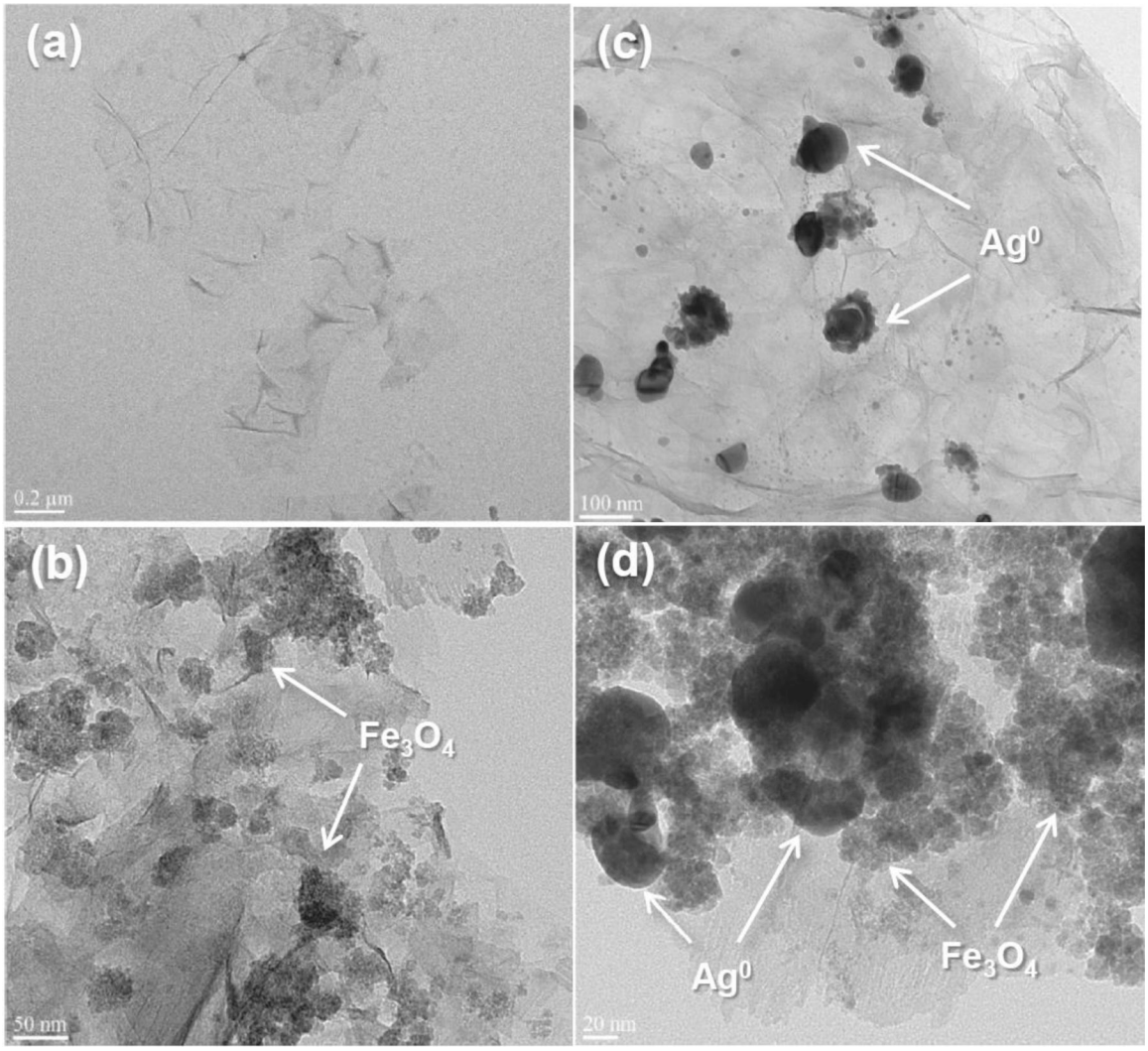

Fig. 1.

Representative transmission electron microscopy images of (a) rGO, (b) rGO/magnetite, (c) rGO/silver, and (d) rGO/magnetite/silver nanohybrids.

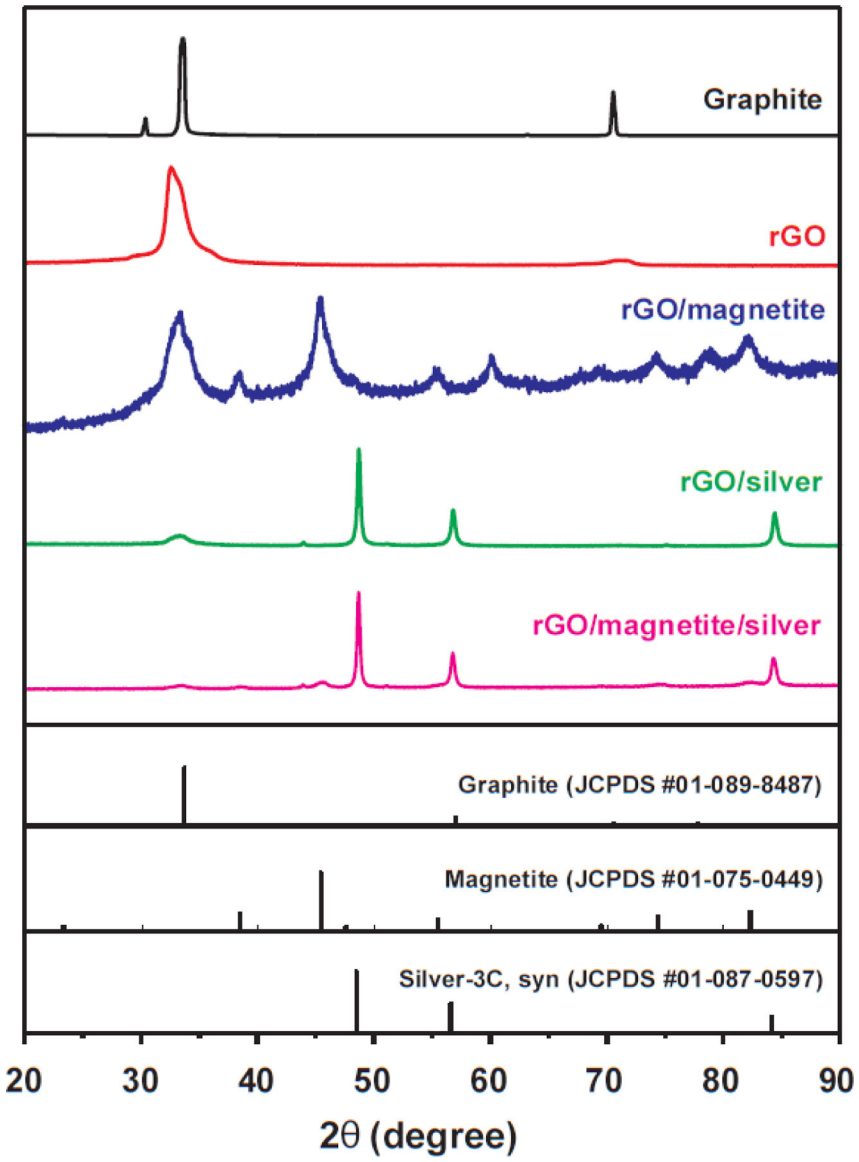

Fig. 2.

XRD patterns of pristine graphite, magnetite, silver, rGO, rGO/magnetite, rGO/silver, and rGO/magnetite/silver nanohybrids.

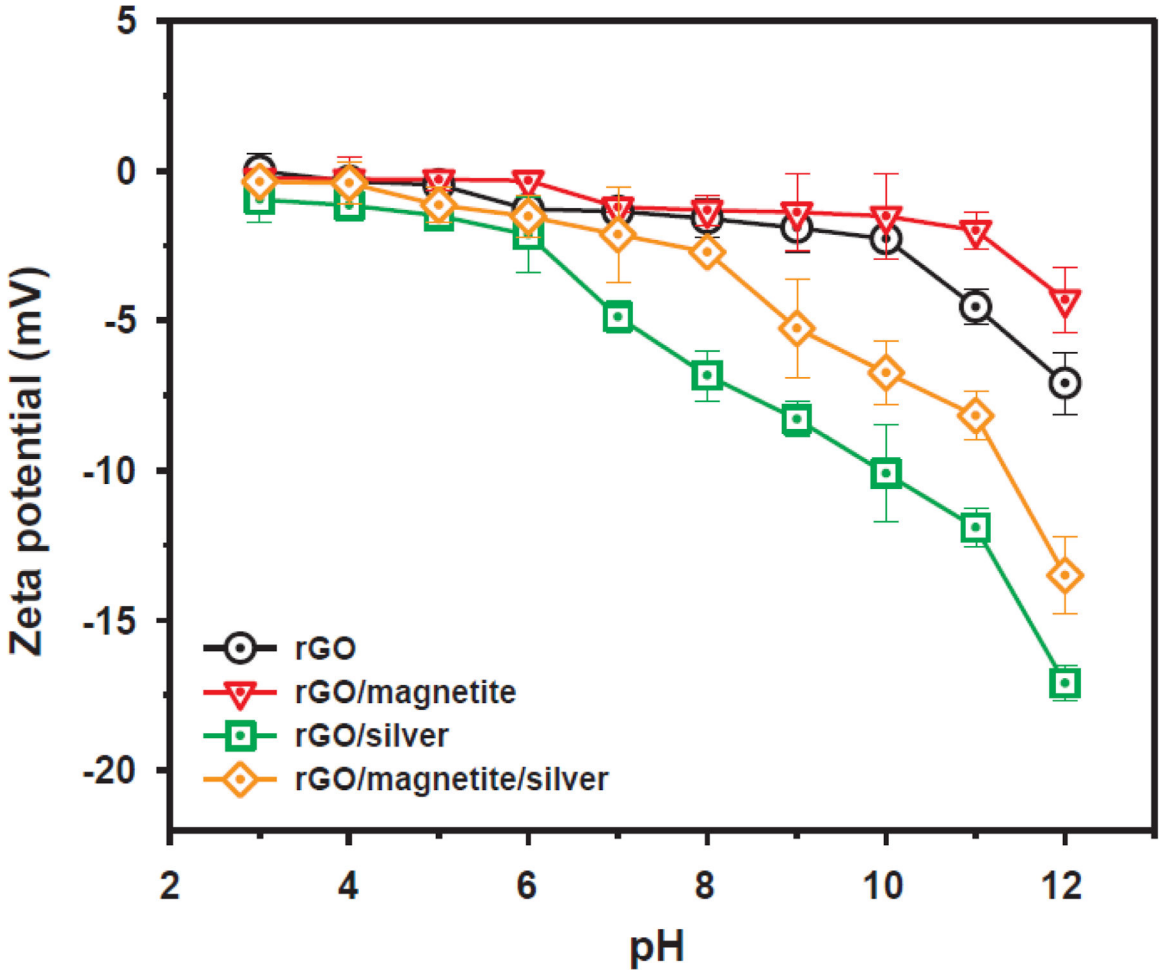

Fig. 3.

Variations in the surface (zeta) potential of rGO, rGO/magnetite, rGO/silver, and rGO/magnetite/silver nanohybrids in water with solution pH at 298 K (adopted from Park et al. [20]). Error bars indicate the standard deviations for at least triplicate measurements.

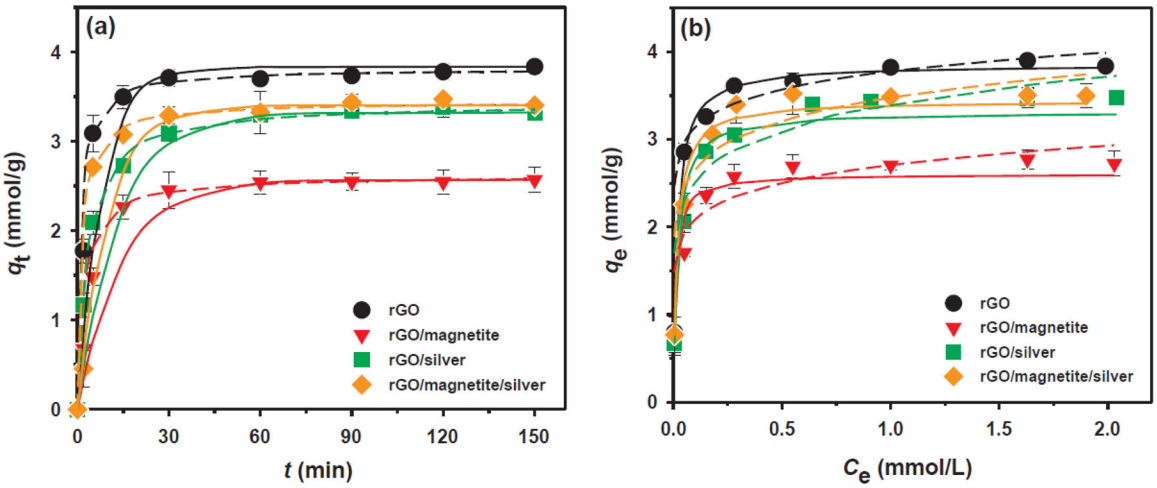

Fig. 4.

(a) Adsorption kinetics and (b) isotherms of Cd(II) ions on rGO, rGO/magnetite, rGO/silver, and rGO/magnetite/silver nanohybrids. The solid and dashed lines represent the pseudo-first-order and pseudo-second-order kinetic models or Langmuir and Freundlich isotherm models fitted results, respectively. Experimental conditions: m/V = 0.2 g/L; initial pH = 4.0 ± 0.1; $[Cd(II)]_0$ = 1 mM, I = 0.01 mol/L $NaNO_3$;

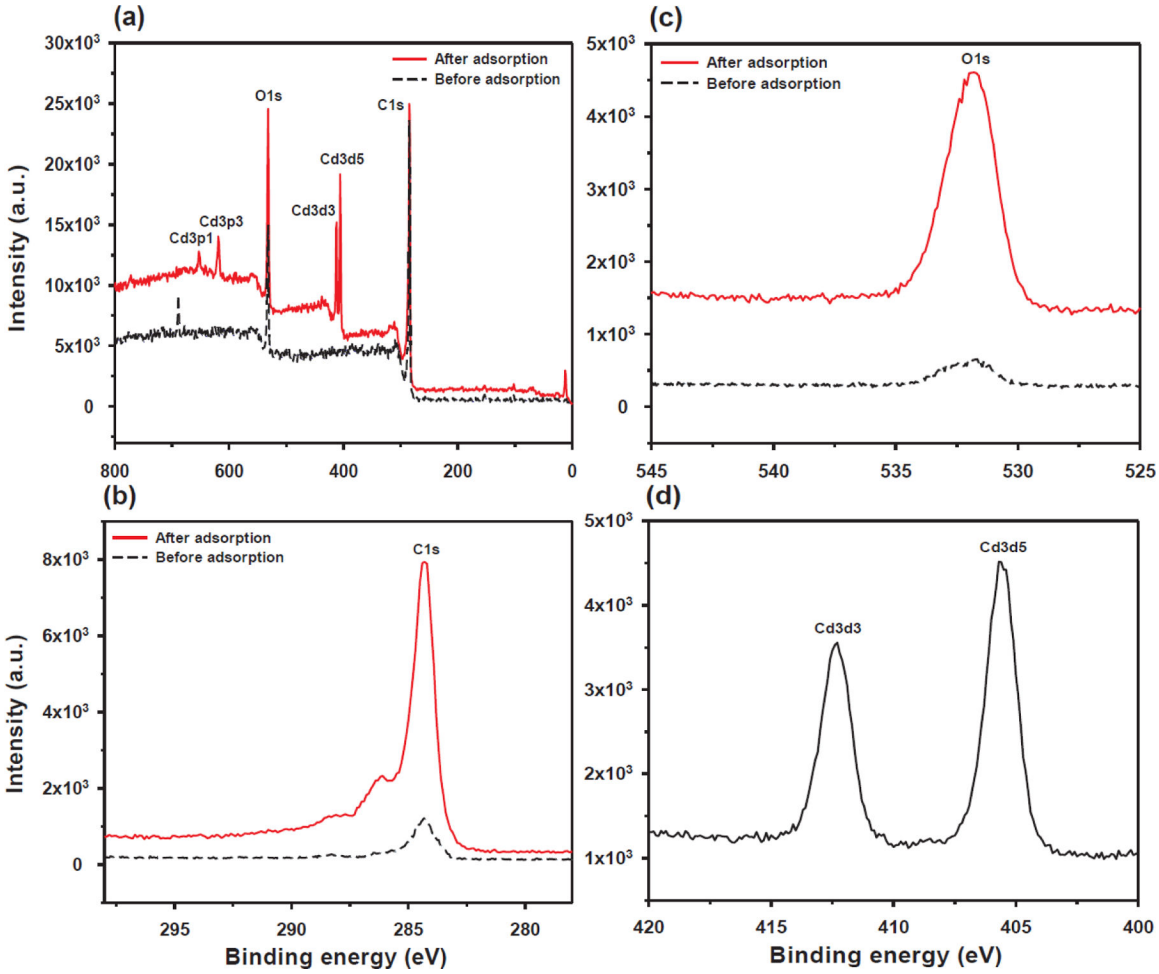

Fig. 5.

(a) X-ray photoelectron spectra survey scans of rGO before and after Cd(II) adsorption, and XPS spectra of (b) C1s, (c) O1s, and (d) Cd3d for rGO before and after Cd(II) adsorption.

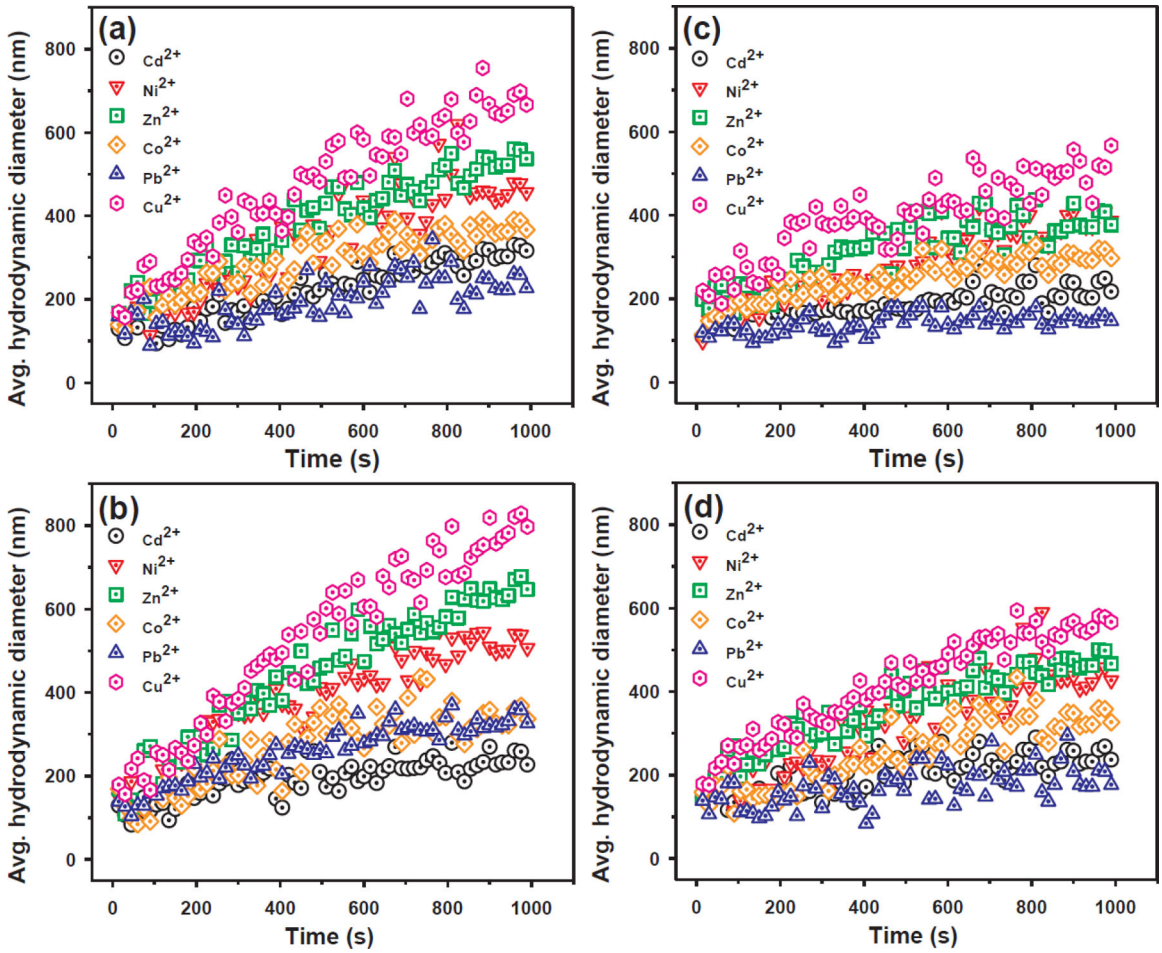

Fig. 6.

Dynamic aggregation history of (a) rGO, (b) rGO/magnetite, (c) rGO/silver, and (d) rGO/magnetite/silver nanohybrids in the presence of different heavy metal ions. Experimental conditions: m/V = 0.2 g/L; initial pH = 4.0 ± 0.1; $[Cd(II)]_0 = [Ni(II)]_0 = [Zn(II)]_0 = [Co(II)]_0 = [Pb(II)]_0 = [Cu(II)]_0$ = 1 mM; I = 0.01 mol/L $NaNO_3$; and T = 298 K.

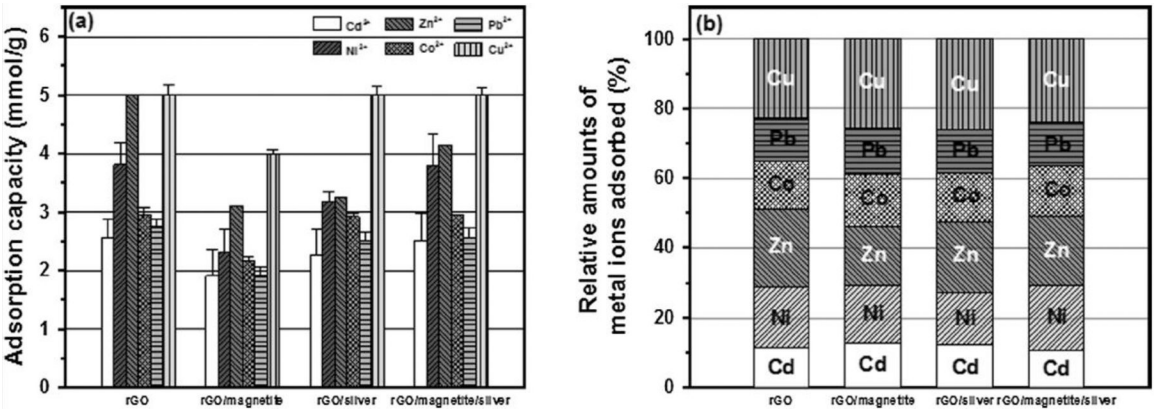

Fig. 7.

(a) Competitive adsorption of Cd(II), Ni(II), Zn(II), Co(II), Pb(II), and Cu(II) on rGO, rGO/magnetite, rGO/silver, and rGO/magnetite/silver nanohybrids and (b) relative amounts of metal ions adsorbed on rGO, rGO/magnetite, rGO/silver, and rGO/magnetite/silver nanohybrids (mole percentage). Experimental conditions: m/V = 0.2 g/L; initial pH = 4.0 ± 0.1; $[Cd(II)]_0 = [Ni(II)]_0 = [Zn(II)]_0 = [Co(II)]_0 = [Pb(II)]_0 = [Cu(II)]_0$ = 1 mM; and T = 298 K.

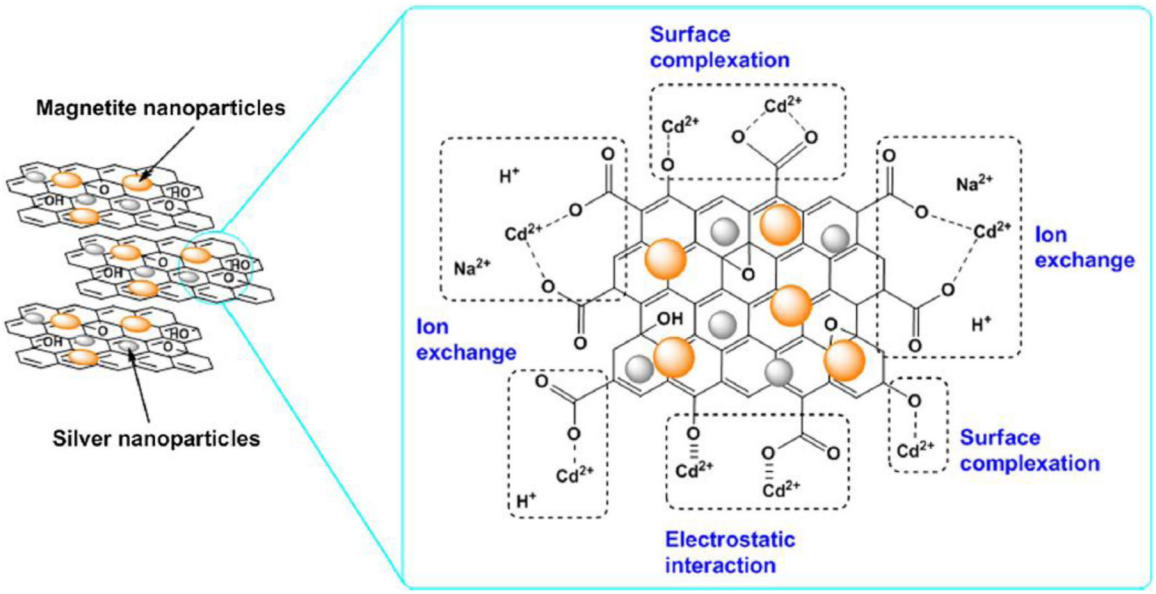

Scheme 1.
Proposed adsorption mechanisms for Cd(II) ions on the rGO/magnetite/silver NH sample.

Table 1.

Comparison of different preparation techniques and adsorption performances of various adsorbents for Cd(II) removal. The adsorbents are arranged according to the development sequence.

Adsorbent	Preparation technique	Adsorption capacity (mmol/g)	Dose (g/L)	pH	Ref.
Oxidized carbon nanotubes (CNTs)	Oxidation of CNTs with HNO_3	0.026	1.5	4.5	[21]
Ethylenediamine-functionalized multi-walled carbon nanotubes (MWNTs)	Chemical modification of MWNTs with ethylenediamine	0.199	0.1	8.0	[50]
Nano zerovalent iron (nZVI)	Bottom-up' method for reducing Fe^{3+} to Fe^0 by $NaBH_4$	6.843	0.5	-	[51]
Fe_3O_4-orange peel powder (MNP-OPP)	Co-precipitation of orange peel with Fe_3O_4 nanoparticles	0.635	0.1	7.0	[52]
Graphene oxide (GO)	Oxidation of graphene with $K_2Cr_2O_7$	4.715	0.1	5.0	[34]
α-ketoglutaric acid-modified magnetic chitosan (α-KA-Fe_3O_4/CS)	Synthesis of Fe_3O_4/CS composite through co-casting method and modification with α-ketoglutaric acid	1.789	1.3	6.0	[53]
3D sulfonated reduced graphene oxide (3D-SRGO)	Direct anchoring of sulfonic acid-containing aryl radicals to rGO	2.089	0.1	6.0	[12]
Nano zerovalent iron supported on reduced graphene oxides (NZVI/rGOs)	Synthesis of NZVI/rGOs using modified Hummers method followed by H_2/Ar plasma technique	3.787	0.1	5.0	[54]
NaOH-impregnated biochar	Thermal treatment of torrefied loblolly pine chips at 300 °C for 15 min and activation with NaOH	1.488	0.05	7.5 ± 0.1	[9]
Potassium (K)-rich biochar	Slow pyrolysis of banana peels and cauliflower leaves at 600 °C for 2 h	1.079	2.5	-	[55]
rGO/magnetite/silver	Oxidation of graphene with $KMnO_4$ and modification of GO with $FeCl_3 \cdot 6H_2O$ and $AgNO_3$	3.441	0.2	4.0 ± 0.1	This study